Journal of the Ceramic Society of Japan (2026), Advance Publication by J-stage
DOI https://doi.org/10.2109/jcersj2.25148

JCS-Japan

FULL PAPER

Tracing nitridation reaction toward efficient production of oxynitride glasses as hosts for bright luminescence centers

Xun Liu[1,2], Takeo Ohsawa[1], Noriko Saito[1], Kohsei Takahashi[1], Takashi Takeda[1], Kenzo Deguchi[1], Shinobu Ohki[1], Tetsuo Kishi[3], Tetsuji Yano[3], Hiroyo Segawa[1,3,†] and Naoki Ohashi[1,2,4]

[1] National Institute for Materials Science (NIMS), 1–1 Namiki, Tsukuba, Ibaraki 305–0044, Japan
[2] Interdisciplinary Graduate School of Engineering Sciences, Kyusyu University, 6–1 Kasugakoen, Kasuga, Fukuoka 816–8580, Japan
[3] Department of Chemistry and Materials Science, Graduate School of Science and Engineering, Institute of Science Tokyo, 2–12–1 Ookayama, Meguro-ku, Tokyo 152–8552, Japan
[4] Materials DX Research Center for Element Strategy, Institute of Science Tokyo, 4259 Nagatsuta, Midori-ku, Yokohama 226–8503, Japan

Europium-doped oxynitride glass powder (Sr–Si–Al–O–N) was synthesized by a sol–gel method followed by ammonolysis to investigate the effect of the ammonolysis conditions on the structure and properties of the glass powder. In particular, the effect of the ammonia gas flow rate during nitridation was studied. The effective nitrogen concentration (N_{eff}) in the obtained powder, analyzed by X-ray fluorescence, increased with an increase in the flow rate, and the results of X-ray photoemission, nuclear magnetic resonance, and Fourier transform infrared (FT-IR) spectroscopy measurements indicated that the population of Si–N bonds increased with an increase in N_{eff}. However, the presence of hydrogen-terminated structures, such as $–NH_n$, in the powder with high N_{eff} was confirmed by FT-IR measurements. The presence of hydrogen-terminated structures, such as $–Si–NH_n$, and the thermal stability of these hydrogen-related structures were further investigated by thermal analyses, including thermal desorption measurements, which suggested that hydrogen-terminated structures can be easily formed during the nitridation of the gel and that the formation of hydrogen-terminated structures inhibits the polymerization of the glass structures.

Key-words : Oxynitride glass, Nitridation, Ammonolysis, Sol–gel method, Europium, Luminescence

[Received October 29, 2025; Accepted December 6, 2025; Published online January 16, 2026]

1. Introduction

In recent years, a major focus in materials science has been the exploration of compounds with complex chemical compositions to realize further higher materials performance. The term "high-entropy alloys"[1,2] is highlighted in metallurgy, and "mixed-anion compounds"[3–5] is another encouraging term for inorganic functional materials. Because atomic numbers are integers, alloying and making solid solutions are the most common approaches for achieving precise control of material properties. Many examples of mixed-anion compounds are available. For instance, oxychalcogenides[6] and oxyhalides[7] have been considered for electro-optical coupling because anion mixing is a possible way to introduce the lattice distortions associated with electric dipoles. Similarly, many phosphors are produced by anion mixing to form specific coordination structures around luminescent centers.[8–11]

Two categories of mixed-anion compounds exist: those involving isovalent anion mixing, such as oxychalcogenides, and those involving heterovalent anion mixing, such as oxyhalides. Charge compensation is an issue in heterovalent anion mixing. Simultaneous cation substitution to maintain charge neutrality and crystal structure,[12–15] or modification of the crystal structure to allow changes in the cation/anion ratio,[16–18] is necessary to form heterovalent anion exchanges, both of which are required to form heterovalent mixed-anion compounds.[19] Because the valence band in inorganic compounds is usually formed with the valence electrons of anions, heterovalent anion mixing directly impacts the electronic structure of the valence band.[15,20] Hence, state-of-the-art techniques are sometimes required for the synthesis of heterovalent anion mixtures.[19,21–24] Despite the difficulties in synthesis, heterovalent anion mixing extends the ability of material design. Mixed-anion compounds in electrochemical systems are expected to modify the electronic and chemical properties of the materials. Anion exchange affects the most fundamental parameters, for example, work-function and electron affinity,[20,25] which are essential in electrochemistry.

This study focuses on oxynitride glasses, a family of mixed-anion systems. The incorporation of nitrogen into oxide glasses is a feasible approach in glass technology.[26]

[†] Corresponding author: H. Segawa; E-mail: SEGAWA.Hiroyo@nims.go.jp

As nitrides are expected to exhibit higher mechanical strength and melting temperatures than oxides, oxynitrides have been highlighted as potential structural materials for high-temperature applications.[27,28] Hence, the enhancement of the mechanical and chemical properties is the purpose of oxynitride glass development. We are interested in the development of host materials for luminescent lanthanide centers. Oxynitride glasses are expected to become outstanding host materials for luminescent lanthanide centers,[29–31] assuming an analogy to crystalline oxynitride phosphors such as $M_xSi_{12-(m+n)}Al_{m+n}O_nN_{16-n}$ ($M =$ lanthanide), conventionally called SiAlON.[8,32,33] However, ordinary glass processes, including melting and casting, are unlikely to be appropriate for oxynitride glass production, because stable melts are rarely formed.[26,34] Thus, nitridation of conventional oxide glass has been considered a conventional route to form oxynitride glasses.

As mentioned above, the high-temperature stability of nitrides and oxynitrides is an evident advantage for their application. However, their very slow ion diffusivity, which is the origin of their high-temperature stability, causes difficulties in their fabrication. To the best of our knowledge, reports on the nitrogen ion diffusion coefficient in nitrides are rare because extremely low diffusivity causes technical difficulties.[35,36] Melting, followed by casting, is the most conventional method for fabricating glass. Shaping by casting is the most obvious advantage of glass materials. However, formation of molten oxynitride glasses is very difficult.[37–42]

To overcome such difficulties, gels and porous nanogranular oxides have been considered as source materials for the synthesis of oxynitride glasses.[43–45] The small grain size and large surface area of the oxide grains should enhance nitridation with a very large surface area and shorten the diffusion path for the completion of nitridation.[21] However, our previous demonstration suggested that a relatively long heat treatment (e.g., 24 h) is necessary to obtain a stable oxynitride glass structure and that the very slow structural relaxation in oxynitride glasses is still an issue for their preparation of oxynitride glasses. Hence, we were motivated to trace the nitridation behavior during ammonolysis of oxide gels with the aim of proposing an efficient nitridation process to produce oxynitride glass powders with relatively short reaction times. In particular, we focused on the effect of ammonia gas flow rate during ammonolysis to elucidate the reaction kinetics.

In this study, Eu-doped Sr–Si–Al–O–N glass was investigated as a case study to elucidate the nitridation behavior of xerogels. The ammonolysis conditions were varied to achieve variations in the nitrogen concentration in the resultant materials, and their chemical states were characterized by spectroscopic techniques, including magic-angle-spin nuclear magnetic resonance (MAS-NMR), Fourier transform infrared spectroscopy (FT-IR), and X-ray photoelectron spectroscopy (XPS), in addition to thermal analysis, that is, thermal gravimetry (TG) and thermal desorption spectrometry (TDS). Luminescence originating in the Eu centers was also studied as a probe to observe variations in glass structures.

2. Experiment

Glass powder samples, $(Si_{0.85}Al_{0.15}Sr_{0.10}Eu_{0.03})$–O–N, were synthesized through a two-step process, that is, the preparation of xerogels by a sol–gel process and subsequent nitridation by ammonolysis. The sol–gel process was initiated by the hydrolysis of tetraethoxysilane (TEOS, >95 %, Fujifilm) using an aqueous solution of nitric acid, and the TEOS:H_2O:HNO_3 ratio was set at 1:4.7:0.001 in molar ratio. After stirring the obtained silica sol for 1 h, a solution mixed with ethanol and N,N-dimethylformamide (DMF, >99.5 %, Wako), in which $Al(NO_3)_3{\cdot}9H_2O$ (99.9 %, Fujifilm) and $Eu(NO_3)_3{\cdot}6H_2O$ (99.9 %, Wako) were dissolved, was added to the silica sol and the mixture was stirred for 15 min.[42] Subsequently, an aqueous solution containing $Sr(NO_3)_2$ (>98 %, Wako) was added to the mixture to set the TEOS:H_2O = 1:9.4 and was stirred for 15 min. Finally, the nominal composition of the sol was TEOS:EtOH:DMF:H_2O = 1:4.7:4.7:14.1 in molar fraction, and the nominal composition of the metallic elements in the sol was Si:Al:Sr:Eu = 85:15:10:3. The obtained sol was dried at 80 °C for approximately 3 days to form transparent solidified gels. The dry gel was crushed in an agate mortar for several minutes.

The nitridation of the gel powder was examined by ammonolysis using a tube furnace with a pure silica glass tube. Highly purity ammonia gas (NH_3, 99.999 %, Showa Denko K.K.) was supplied at flow rates (Φ_{AM}) of 20, 100, 300, and 500 cm^3/min to evaluate the effect of gas flow on the nitridation behavior. Before introducing the NH_3 gas, the furnace tube was evacuated to reduce the oxygen partial pressure to the lowest possible level. NH_3 gas was introduced into the furnace prior to heating and flowed continuously through the high-temperature process. The furnace was heated to 1000 °C at the ramping rate of 330 °C/h unless otherwise noted and held at 1000 °C for 12 h. Hereafter, the samples are identified by the codes P020, P100, P300, and P500 with Φ_{AM} during ammonolysis of 20, 100, 300, and 500 cm^3/min, respectively. In addition, a subset of P500 samples was prepared at a slower ramping rate of 110 °C/h to elucidate the role of the calcination process. Because organic decomposition and dehydrogenation occur during heating, the ramping rate is expected to influence the chemical states of the resultant samples. These samples are denoted as P500SR. Notably, the exhaust gas from the furnace during ammonolysis was analyzed using gas chromatography to estimate the actual gas composition in the furnace.

In addition to the powders synthesized via ammonolysis, two reference powders were prepared. One reference powder, identified by PwO, was prepared by oxidizing the precursor gel at 1000 °C for 6 h in air atmosphere. The other one, identified by PwH, was prepared in two steps as follows: First, the gel was heated in air atmosphere at 1000 °C for 4 h and subsequently heated in H_2 gas stream at 1000 °C for 2 h.

Absence of crystalline phases in the obtained powder was confirmed by powder X-ray diffraction (XRD) with Cu Kα radiation using a MiniFlex diffractometer (Rigaku Co. Ltd.). The average chemical composition was analyzed via X-ray fluorescence (XRF) using a ZSX Primus II spectrometer (Rigaku Co., Ltd.) with semi-qualitative analysis functions. Spectroscopic characterizations were performed to elucidate the coordination structures formed in the samples. The vibrational modes of the samples were characterized using a Nicolet iS50FT-IR spectrometer (Thermo Fisher Scientific Inc.). For most FT-IR measurements, the powder samples were pelletized with KBr powder and the pellets were dried by heating at 150 °C for 15 min in order to avoid the contribution of extrinsic water to the vibrational spectra. In addition, the attenuated total reflection (ATR) technique was adopted for the FT-IR measurements, and a diamond prism was utilized to avoid the effects of water adsorption on the KBr powder. The chemical state of every element in the resultant glass powders was characterized by XPS, using a PHI-Quantes spectrometer (ULVAC-PHI, Inc.) equipped with a monochromatic Al Kα X-ray generator. The pressure in the XPS chamber was maintained at 1×10^{-8} Torr during measurements and a charge neutralizer was used to enable measurements for the insulating powders.

The local structures around Si and Al were also investigated using MAS-NMR. The MAS-NMR signal of ^{27}Al at 208.49 MHz was studied with a JNM-ECZ 800 MHz spectrometer (JEOL Ltd.) and the samples were set in a 3.2 mm double-tuned broadband probe spinning at 20 kHz. An aqueous solution of $AlCl_3$ (1 mol %) was used as a reference for the ^{27}Al MAS-NMR measurements. The pulse width of 0.6 µs was used, which was one-third of $\pi/2$ (= 1.8 µs) in the solution, the relaxation delay was set at 1.0 s, and the chemical shift was calibrated by setting the chemical shift of the solution at 0 ppm. Further, high-resolution ^{29}Si signal was collected by the dipolar-decoupling-magic-angle-spinning (DDMAS) procedure at 99.38 MHz with a JNM-ECA 500 MHz spectrometer (JEOL Ltd.), and tetramethylsilane was used as an external standard. The samples were packed in a 4 mm zirconia rotor, the spin frequency was set at 10 kHz, and the pulse width and relaxation delay were set at 3 µs of $\pi/2$ pulse and 120 s, respectively.

Thermal analysis was performed by TDS and differential thermal analysis (DTA). TG–DTA measurements were performed with a conventional instrument (TG–DTA 2000SA, Bruker Japan K.K.) under N_2 gas stream at 150 cm^3/min, using Al_2O_3 powder as a reference. For TG–DTA measurements, approximately 20 mg powder samples were set in a Pt pan and heated at a ramping rate of 10 °C/min. TDS spectra were measured using an EMD-WA1000S system (ESCO, Ltd.). The powdered samples were packed with Pt foil to avoid reaction with the crucible made of silicon carbide. The base pressure in the analytical chamber was maintained at 10^{-9} Torr or lower prior to heating. The sample temperature was elevated to 1000 °C at a ramping rate of 3 °C/min, held at 1000 °C for 3 h, and cooled down to room temperature. This temperature program was repeated twice to ensure complete desorption during the first heating cycle. The P500SR sample after the TDS measurement was analyzed using XPS again to examine the changes in the chemical state during the measurement.

The photoluminescence (PL) and photoluminescence excitation (PLE) spectra were obtained using an F-7100 fluorescence meter (Hitachi High-Tech Corp.). The PL spectra were excited by UV light at $\lambda = 300$ nm, and the intensity of the PLE spectra was monitored at the wavelength of maximum PL intensity. In addition, the quantum efficiency (QE) of the luminescence was measured using a QE-2100 spectrometer (Otsuka Electronics Co., Ltd.) according to the literature.[9] All optical measurements were performed at room temperature.

3. Results and discussion

The XRD patterns of the samples after ammonolysis are shown in Fig. S1. Except for P020, all samples remained amorphous after ammonolysis. The XRD pattern of P020 exhibited sharp diffraction peaks assignable to crystalline cristobalite, indicating insufficient NH_3 flow, that is, residual oxygen gas in the furnace, resulting in crystallization. The actual atmosphere in the furnace during ammonolysis, shown in Fig. S2 (Supporting Information), indicated that the P_{O_2} in the furnace with low Φ_{AM} was relatively high. It is also noteworthy that the halo pattern in the XRD profiles showed shift and broadening with Φ_{AM}. Because the halo pattern correlates with the short-range arrangement of atoms in glass,[46] it is presumed that glass structures are responsible for Φ_{AM}.

The effective nitrogen concentration (N_{eff}) values, as defined by Eqs. (1) and (2),[31] were evaluated from the results of the XRF analysis and are shown in **Fig. 1**. Assuming stoichiometry (formal charge of the constituent elements, particularly Eu^{2+}) in the resulting samples, the sample composition can be expressed by Eq. (1), and, hence, N_{eff} was calculated using Eq. (2) from the experimentally observed nitrogen concentration, [N], and oxygen concentration, [O].

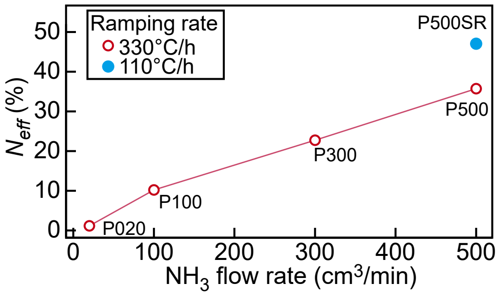

Fig. 1. Nitrogen contents in the synthesized powder versus the ammonia flow rate (Φ_{AM}) on preparation. The powders are identified by Pn where n corresponds to Φ_{AM}. Blue and red symbols distinguish the ramping rate in the nitridation process.

$$\begin{aligned}
&\mathrm{Si_{0.85}Al_{0.15}Sr_{0.10}Eu(II)_{0.03}O_{2.055}} + \frac{1.370N_{\mathrm{eff}}}{2}\mathrm{N_2} \\
&\quad\rightarrow (1 - N_{\mathrm{eff}})(\mathrm{Si_{0.85}Al_{0.15}Sr_{0.10}Eu_{0.03}O_{2.055}}) \\
&\qquad + N_{\mathrm{eff}}(\mathrm{Si_{0.85}Al_{0.15}Sr_{0.10}Eu_{0.03}N_{1.370}}) \\
&\qquad + \frac{2.055N_{\mathrm{eff}}}{2}\mathrm{O_2} \qquad (1)
\end{aligned}$$

$$N_{\mathrm{eff}}\ (\%) = \frac{[\mathrm{N}] \times 3}{[\mathrm{N}] \times 3 + [\mathrm{O}] \times 2} \times 100 \qquad (2)$$

The monotonic increase of N_{eff} with Φ_{AM} looks reasonable, as Φ_{AM} represents nitridation activity. As presented in Fig. S2 in Supporting Information, the actual ammonia partial pressure in the furnace increased with the increase in Φ_{AM}.

Notably, the charge compensation assumed in Eq. (1) is not satisfied with the obtained powder. In the PwO powder prepared by firing in air, the XRF analysis results suggested a slight anion (oxygen) excess under the assumption of an ordinary formal charge, as presented in Table S1. This indicates that some cations that cannot be detected by XRF exist in the obtained powder to satisfy charge neutrality. Because the instrument has no sensitivity to very light elements, that is, H–Be, we could not analyze the hydrogen concentration with the current setup. This implies that the presence of hydrogen-related components is a possible explanation for the observed anion excess. Hence, the splitting of the –Si–O–Si bond in the manner of Eq. (3), for instance, is a reasonable understanding of the excess oxygen in PwO.

$$[\text{–Si–O–Si–}] + \mathrm{H_2O} \rightarrow [\text{–Si–O–H}] + [\text{H–O–Si–}] \qquad (3)$$

The degree of anion excess was more obvious in the sample prepared with higher Φ_{AM}, for example, P500SR. As can be observed in Table S2, the tendency of anion excess was more obvious in the powders prepared with higher Φ_{AM}, which was confirmed from the results of XRF analyses. Hence, it is also presumed that the breaking of bonds in the glass structure, in the manner of Eq. (4), is a possible consideration.

$$\begin{aligned}
&[\text{–Si–N–Si–}] + \mathrm{NH_3} \\
&\quad \rightarrow [\text{–Si–N–H}] + [\text{H–N–Si–}] + \frac{1}{2}\mathrm{H_2} \qquad (4)
\end{aligned}$$

The possibility of these terminal, nonbridging structures will be discussed further, along with the results of other measurements.

Because the presence of –NH and –OH groups was not assumed in Eqs. (1) and (2), the N_{eff} values determined from the total oxygen [O] and nitrogen [N] concentrations may differ from those in the original definition. However, for convenience, we will still use the N_{eff} value determined from total [O] and [N] as a measure for the degree of nitridation.

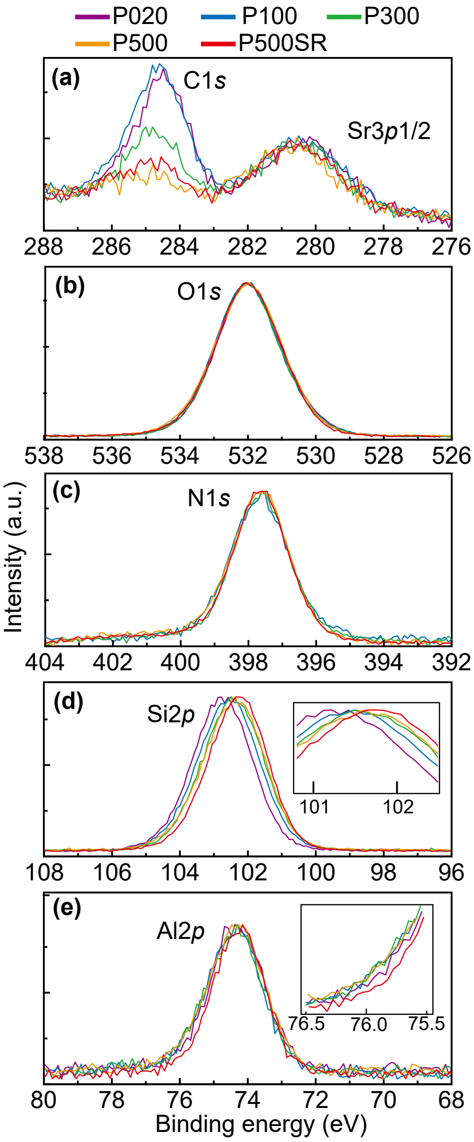

Fig. 2. XPS spectra of the samples after ammonolysis with different ammonia flow rates. The sample identifier, P*n*, indicates powder prepared with ammonia flow rate at *n* $\mathrm{cm^3/min}$. The binding energy is normalized by locating the O1*s* peak at 532 eV. Part of the spectra are magnified in the insets.

The results of the XPS measurements are shown in **Fig. 2**. As a charge neutralizer was used to enable XPS measurement by suppressing charging due to photoionization, calibration of the electron binding energy (E_{b}) was necessary for sample-to-sample comparison. In this study, the binding energies were normalized by referencing the O1*s* core-level peaks of each sample instead of E_{b} of the C1*s* core-level peaks. As shown in Fig. 2(a), the spectral profile for the C1*s* core-level region is broad and asymmetric, which indicates that the composition of carbon-related impurities is very complex and that these peaks are not suitable for E_{b} calibration. Hence, E_{b}s were calibrated by locating the O1*s* peak at 532 eV, which is close to the typical E_{b} for silicate glass reported in some studies.[47,48] As shown in Fig. 2(b), which presents the O1*s* spectra after calibration, the spectral shape of O1*s* does not change with Φ_{AM}. As neither broadening nor splitting of the O1*s* peak due to differences in preparation conditions was observed, it seems that the chemical state of oxygen is common to all powders in this study. Hence, usage of O1*s* peaks for calibration seems more reliable than usage of C1*s* peaks, and the chemical state of the other elements is characterized by E_b difference between the focused element and oxygen.

Next, we focus on the N1*s* core-level spectra. As shown in Fig. 1, N_{eff} in P020 was very low; consequently, the N1*s* peak intensity of P020 was very weak and was not available for discussion. Thus, the N1*s* spectra of P020 was omitted from Fig. 2(c). For the other samples, the N1*s* peak is located at approximately 397.5 eV and exhibits a very similar profile, indicating that the chemical states of nitrogen in these samples are close to each other. If we assume that energy calibration locating the O1*s* peak at 532 eV is quite reasonable, the observed N1*s* XPS signal is very similar to that of crystalline silicon nitride, which normally appears at $E_b \approx 398$ eV.49) Regardless of the E_b calibration issues, it is evident that the shapes of N1*s* and O1*s* peaks merely changed with Φ_{AM}, and that the difference between E_b of O1*s* and N1*s* is constant in all samples. Notably, the energy difference between N1*s* and O1*s* (134 eV) observed in this study is constant against variation of Φ_{AM} and is the same as that in other oxynitrides, such as $SrNbO_2N$.50) In general, the XPS peak energies show an obvious shift not only due to changes in the chemical state but also due to a shift in the Fermi energy.51,52) Thus, the energy difference between O1*s* and N1*s* is a good measure for the chemical state analyses of oxynitrides. Hence, we can safely conclude that the chemical states of oxygen and nitrogen are unchanged with Φ_{AM} from the viewpoint of a photoemission study. The value of N_{eff} determined from XPS measurements is shown in Supplemental Information (Fig. S3). It was similar to N_{eff} obtained from XRF measurements, showing the increase of N_{eff} with Φ_{AM}. The difference in the N_{eff} behavior shown in Figs. 1 and S3 was likely due to probing depth, high surface sensitivity of XPS and choice of the relative sensitivity factors for convertion of XPS peak intensity to composition.

As described above, the XRF analyses indicated an excess of anions compared with those in the assumed composition expressed by Eq. (1). Notably, the variation of N_{eff} with Φ_{AM} determined by XPS (Fig. S3) was consistent with that analyzed by XRF. Hence, the excess of anions is a feasible characteristic of the powder prepared with high Φ_{AM}. Assuming that Eqs. (3) and (4) are applicable, two or more types of oxygen and nitrogen are present, for example, bridging oxygen, such as –Si–O–Si–, and terminal oxygen, such as –Si–O–H. However, the O1*s* and N1*s* core-level spectra appeared to be of a single origin. Tentatively, we assume that anions at different coordination positions, such as the terminal and bridging positions, cannot be resolved by the XPS core-level spectra obtained in this study, and that the intensity of those peaks represents the total concentration of the corresponding elements.

While the E_b difference between O1*s* and N1*s* was merely changed with Φ_{AM}, the XPS peak for some cationic elements showed shift with Φ_{AM}. Indeed, E_b of the Si2*p* peaks shifted with Φ_{AM} as shown in Fig. 2(d). Corresponding to the monotonical increase in N_{eff} with increasing Φ_{AM}, the E_b at Si2*p* peak showed monotonical shift to the lower E_b direction with the increase in Φ_{AM}. This result suggests that the chemical state of Si is strongly affected by N_{eff}, which reproduces the effect of N_{eff} on the XPS profile of oxynitride glasses, as shown in our previous study on Si–Al–Sr–Eu–O–N glass films.30) As the present study employs the O1*s* core-level for energy calibration, the correct expression for the Si2*p* XPS peak is that the energy difference between Si2*p* and O1*s* is parallel to that between Si2*p* and N1*s*. This indicates that the ionicities of Si–O and Si–N were enhanced with an increase in N_{eff}.

In contrast to the behavior of the Si2*p* XPS peaks, the Al2*p* peak profile [Fig. 2(e)] was almost the same for all the samples, regardless of Φ_{AM}. When we carefully compared the Al2*p* peak profiles, the effect of Φ_{AM} onto the peak profile of Al2*p* was found at the tail at a higher E_b side, as shown in the inset. It appears that the spectral tail develops with an increase in Φ_{AM}. Because the presence of a spectral tail in the Al2*p* region due to ammonolysis was more evident in our previous study on Si–Al–Sr–Eu–O–N glass films,30) the behavior of the spectral tail of Al2*p* should be attributed to the effect of nitridation. Notably, the effect of nitridation on the peak shape of Al2*p*, development of tail at higher E_b direction with Φ_{AM}, was opposite to that of Si2*p* shift to lower E_b direction with the increase in Φ_{AM}. The effect of Φ_{AM} on the peak profile of Sr3*p* at approximately $E_b = 280.5$ eV [Fig. 2(a)] seemed to be rather similar to that of Al2*p*. The Sr3*p* peak exhibited a slight shift to a higher E_b direction with increasing Φ_{AM}. As the magnitude and direction of the peak shift due to Φ_{AM} were different from element to element, neither charging nor the shift of Fermi level should be the reasons for the XPS peak shift. Hence, the results suggested that the chemical state of cations systematically changed with the increase in N_{eff} resulting from the increase in Φ_{AM}.

Figure 3(a) shows ^{29}Si NMR spectra of the powder prepared with different Φ_{AM}. As shown in this figure, the spectral profile changed drastically with Φ_{AM}. An exceptionally sharp peak found in the spectrum of P020 at approximately −110 ppm was assigned to the crystalline phase, cristobalite, formed during ammonolysis. As the nitrogen content increases due to a large Φ_{AM}, signals at higher chemical shift become obvious and the whole spectra becomes broad. Previous NMR studies of several oxynitride and nitride compounds indicated that the ^{29}Si spectra of the $[SiO_xN_y]$ coordination structures showed a larger chemical shift with an increase in the fraction of nitrogen involved.53–55) According to those previous studies, the increase in N_{eff} with the increase in Φ_{AM} can be attributed to the increase in both the population of $[SiO_xN_y]$ and y in $[SiO_xN_y]$.

On the other hand, the profile of ^{27}Al NMR spectra shows less obvious changes with N_{eff}, as can be observed in Fig. 3(b). As the peak at 52–57 ppm has been identified as tetrahedral $[AlO_4]$ coordination56,57) most of the aluminum is presumed to occupy tetrahedral sites coordinated

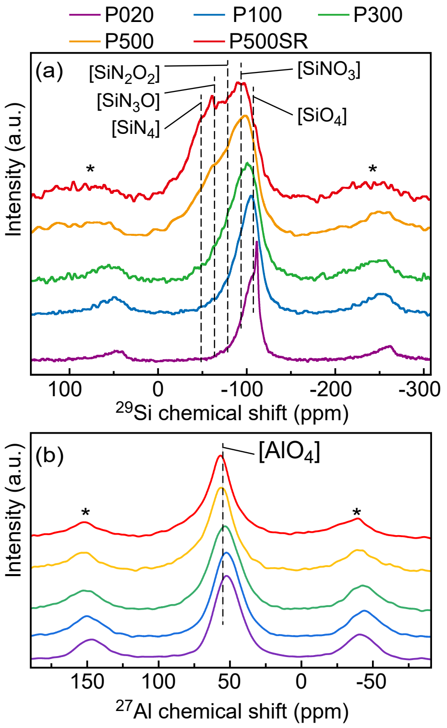

Fig. 3. NMR signal of ^{29}Si (a) and ^{27}Al (b) of the synthesized powder prepared under different ammonolysis conditions. The powder was identified by Pn, where n is the flow rate of ammonia (cm^3/min) during ammonolysis.

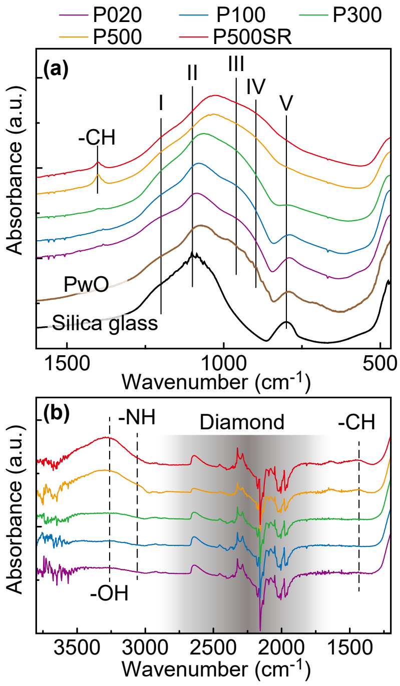

Fig. 4. FT-IR spectra of the powder samples after ammonolysis with different flow rates of the ammonia stream. The sample identifier, Pn, indicates the powder prepared by ammonolysis with flow rate of n cm^3/min. Lower wavenumber range measured with the conventional transmission mode (a), and higher wavenumber range measured with the ATR mode with a diamond prism (b).

with the four oxide ions. It is also notable that octahedral [AlO$_6$] and hexahedral [AlO$_5$] are rarely formed, as aluminum-oxygen polyhedra with higher coordination numbers should cause peaks in the range of lower chemical shifts.[58)]

The XPS and NMR spectra of the samples are consistent. In fact, the Al2p XPS spectra and ^{27}Al NMR spectra did not show an obvious shift resulting from the increase in N_{eff}, whereas the Si2p core-level spectra and ^{29}Si NMR spectra showed a shift with an increase in N_{eff}. Hence, it is evident that the chemical state of silicon is sensitive to N_{eff}, whereas that of aluminum rarely responds to changes in N_{eff}. This tendency has been commonly observed in previous studies on oxynitrides, including silicon and aluminum.[59–61)]

Figure 4(a) presents the FT-IR spectra of the Si–O- and Si–N-related modes. As shown in this figure, the spectra appear to be composed of several peaks, denoted by bands I–V. Peaks centered at approximately 1200 cm^{-1} (band I) and 1080 cm^{-1} (band II) were assigned to the asymmetric stretching mode of –Si–O–Si bonds,[62,63)] and the peak centered at 800 cm^{-1} (band V) was also identified as a symmetric bond stretching mode associated with the –Si–O–Si-forming network structure in the glass.[64)] A comparison between the FT-IR profiles of PwO and silica glass indicated that bands II and V in the current samples presented obvious broadening owing to the addition of Sr and Al. The peak denoted by band-III at approximately 960 cm^{-1}, assignable to the stretching vibration of Al–O–Si bonds,[65)] could appear in the current samples. However, the presence of band III was not evident because of the broadening of band II. In addition to the aforementioned vibrational modes, an additional mode, band IV, was observed in these spectra. According to the literature, the peak at approximately 900–950 cm^{-1}, that is, band IV, can be assigned to the Si–N stretching mode.[66,67)] As the intensity of band-IV seems consistent with N_{eff}, the development of the spectral intensity at approximately 900–950 cm^{-1} can be reasonably attributed to the increase in the population of the Si–N bond. These results are consistent with the results of the XPS and NMR measurements, which indicate that nitride ions preferentially form Si–N bonds. Apparently, the broadening of the NMR signal due to the appearance of the shoulder on the small chemical shift side, the shift of the Si2p XPS peak to a lower E_{b} direction, and the shift of the FT-IR peak from 1080 cm^{-1} to a smaller wavenumber direction arise from the same origin, the increase in nitrogen sitting as the nearest neighbor to silicon.

In addition to the Si–O and Si–N related modes, a peak at approximately 1400 cm^{-1} was found in the FT-IR spectra of P500 and P500SR as shown in Figs. 4(a) and 4(b). Furthermore, broad but obvious peaks at approximately 3200–3600 cm^{-1} were observed in the FT-IR spectra of P500 and P500SR, as shown in Fig. 4(b). These peaks can be assigned to hydrogen-related vibrational modes[68,69)] originating from C–H, N–H, and O–H, as indicated in the figure. As mentioned, actual oxygen partial pressure (P_{O_2})

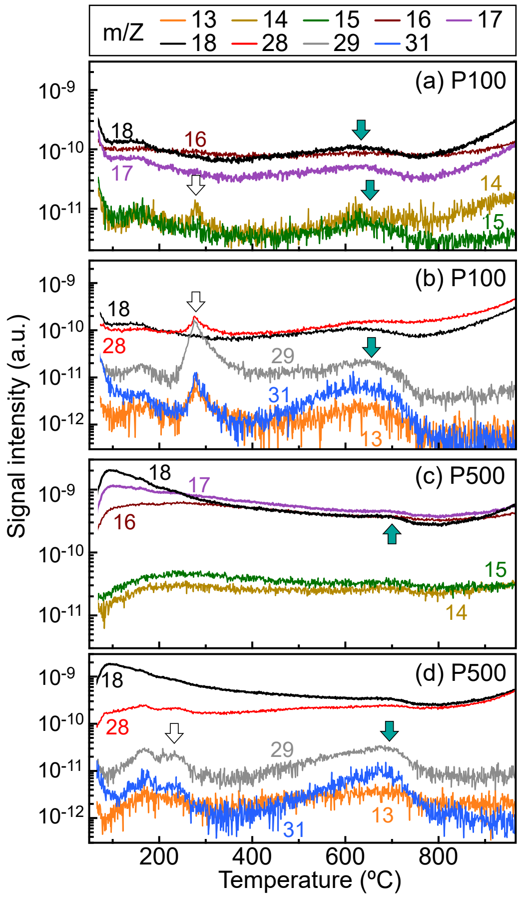

Fig. 5. Thermal desorption spectra of P100 (a and b) and P500 (c and d). The powder was identified by Pn, where n (cm^3/min) is the flow rate of ammonia during ammonolysis. The arrows are guides to eyes.

during ammonolysis was relatively high for smaller Φ_{AM} conditions, for example, $\Phi_{AM} = 100$. As shown in Fig. S2, the concentrations of the residual hydrocarbons in P100 and P300 were reduced by combustion. Meanwhile, very low Po_2 achieved by increased Φ_{AM} should be a reason for the significant amount of residual hydrocarbon. The presence of these C–H, N–H, and O–H-related modes suggests the modification of the glass structure by the formation of hydrogen-terminated structures. This is consistent with the XRF results obtained by assuming the splitting of the glass network structure, as expressed by Eqs. (3) and (4). Notably, our previous study[30)] also indicated the breakage of the glass network structure by excess nitrogen.

Figure 5 shows the TDS spectra of the selected samples, where the recorded signals were labeled by the mass/charge (m/Z) ratio as the output from the quadrupole mass spectrometer. First, we focused on the behaviors of $m/Z = 17$ (violet) and 18 (red). Assuming that these two signals are dominated by $^{16}O^1H$ and $^1H_2{}^{16}O$, they must be parallel to each other. As shown in Fig. 5(a), for P100, the profiles of $m/Z = 17$ and 18 were parallel to each other, and their intensity ratio was close to 1:2 over the entire temperature range. This indicated that these two signals could be attributed to water desorption. However, in Fig. 5(c) for P500, the profiles of $m/Z = 17$ and 18 are not parallel to each other, and the intensity of $m/Z = 17$ is higher than that of $m/Z = 18$ in most temperature ranges. This suggested that the signal for $m/Z = 17$ from P500 was not dominated by $^1H^{16}O$.

By contrast, the profiles of $m/Z = 14$ (yellow) and 15 (green) provide hints for identifying the TDS profiles. For the P100 powder shown in Figs. 5(a) and 5(b), the spectral features of $m/Z = 14$ and 15, such as the peaks denoted by arrows, are also observed in the signal for $m/Z = 13$, 29, and 31. Because $m/Z = 13$, 29, and 31 can be attributed to $^{12}C^1H$, $^{12}C_2{}^1H_5$, and $^{12}C^1H_3{}^{16}O$, respectively, it is presumed that the signals for $m/Z = 14$ and 15 in Fig. 5(a) are dominated by hydrocarbons, that is, CH_2 and CH_3. By contrast, in the P500 shown in Figs. 5(c) and 5(d), the behavior of $m/Z = 14$ and 15 looks similar to that of $m/Z = 17$ but dissimilar to that in $m/Z = 13$, 29, and 31. This indicated that the signals for $m/Z = 14$ and 15 in Fig. 5(c) were not dominated by hydrocarbons. It is reasonable to conclude that the signals for $m/Z = 14$, 15, and 17 from P500 originate from ^{14}N, $^{14}N^1H$, and $^{14}N^1H_3$, respectively. Hence, both P100 and P500 contain $-CH_n$ groups, and P500 specifically contains $-NH_m$ groups.

The intensities of the nitrogen-related signals ($m/Z =$ 14, 15 and 17) in Fig. 5(c) were more than one order of magnitude higher than those of P100 over the entire temperature range, but did not show any obvious peaks (temperature dependency). As most of the nitrogen in P500 forms Si–N bonds, as indicated by the FT-IR and NMR measurements, the very high nitrogen desorption signal can be attributed to the breaking of Si–N bonds. As the intensity of the nitrogen-related signals from P500 was relatively high, even at relatively low temperatures, it is presumed that some of the Si–N bonds formed in P500 are thermally unstable. As nitrogen-related desorption continued at higher temperatures and no obvious peaks were observed, it also indicates that the nitrogen desorption rate from P500 was limited by the rate of out-diffusion in P500. It is likely that various types of Si–N bonds exist in P500.

Subsequent XPS measurements of the P500SR powder after the TDS measurements showed that the nitrogen concentration decreased during the TDS measurements. The N_{eff} value of P500SR after TDS measurement was determined to be 34 % by XPS, whereas that before TDS measurement was 38 %. Although obvious desorption of nitrogen-related fragments was observed in the TDS profile, as described above, the amount of desorption during TDS was limited. A characteristic feature of the powder is that an excess of anions remained in the powder after TDS. The TG/DTA measurements (not shown) also indicated weight loss of P500 and P500SR. The magnitude of the weight loss was only a few percentages of the initial weight. Such a weight change was not sufficiently large to suppress excess anions in the powders. Hence, it was confirmed that excess anions remained even after thermal analysis at high temperatures. The quantity of residual organic components is also an important parameter for characterizing the gel ammonolysis process. Although the desorption of hydrocarbons during TDS measurements is evident and the FT-IR signal originating from hydrocarbons was observed, we do not have sufficient results to discuss the amount of residual hydrocarbons with reasonable accuracy.

Summarizing the above presented results, it is evident that nitrogen was successfully incorporated into the powder by ammonolysis and that P100 and P300 were likely stable oxynitride glasses. Although TDS indicated the presence of reaction residues in these three powders, the magnitude of the weight change measured by TG was negligible, and the ^{29}Si NMR signal was relatively sharp for these three powders. The P020 powder also appeared to be a stable oxynitride, but crystallization during ammonolysis and its low N_{eff} are not very suitable for quantitative discussion. Meanwhile, a tread-off in ammonolysis process was highlighted in the sample prepared with high Φ_{AM}. Incorporation of nitride ion into the gel was evidently enhanced by employing high Φ_{AM} conditions, but it was indicated that obvious anion-excess was achieved by employing high Φ_{AM}.

The very high N_{eff} of P500SR, which was prepared with a very slow ramping rate during ammonolysis, must also be highlighted. In our previous study,30) the effect of the ammonolysis duration on oxynitride glass formation was investigated, and it was found that a shorter ammonolysis period resulted in a higher N_{eff}. In the present study, the slow ramping rate at the initiation of ammonolysis drastically increased N_{eff}. Those results indicate that the incorporation of nitride ions was a rapid reaction in the gel. However, it appears that nitride ions introduced in the early stages of ammonolysis inhibit the formation of stable oxynitride glass structures. We speculate the following reaction:

$$[\text{–Si–(NH}_m)] + [(\text{NH}_n)\text{–Si–}] \rightarrow [\text{–Si–N–Si–}] + \delta \text{NH}_x. \qquad (5)$$

The reaction expressed by Eq. (5) assumes that structures terminated by the N–H groups, such as –Si–(NH_2), were formed at the early stage of nitridation, and that the N–H groups are decomposed to form bridging nitrogen (–Si–N–Si–) for polymerization at higher temperatures. The results of XRF measurement for P500SR (Table S2) indicated presence of hydrogen in the powder after ammonolysis as mentioned above. We considered very slow diffusivity in nitrides and oxynitrides compared to oxides. That should be the case for bulk solid glasses. The current study applies ammonolysis to the gel before polymerization. This is a key for understanding the very quick increase of nitrogen concentration in the present study. The microstructure of the gel, very fine grains with relatively high specific surface area (Fig. S4 in the Supporting Information) should also be a reason for the very fast nitrogen insertion behavior. Those should be the causes for formation of the structure terminated by –Si–(NH_n) at the early stage of ammonolysis.

As the spectral profile of XPS [Fig. 2(d)], NMR [Fig. 3(a)], and FT-IR [Fig. 4(a)] indicated monotonical increase of Si–N bond density with N_{eff}, but it seems those method did not distinguish if Si–N bonds were involved in –Si–(NH_n) or –Si–N–Si–. Hence, it is a very important indication that not only XPS, NMR, and FT-IR but also some additional characterizations are needed to characterize oxynitride glasses in detail.

From these considerations, we speculate that a sufficiently long thermal relaxation time is necessary for completing polymerization to form stable oxynitride glass structures. Indeed, Eq. (5) assumes the presence of two near-terminal structures. When a single terminal structure exists alone and is surrounded by relatively stable bridging structures, the simple removal of the –NH_n groups results in the formation of dangling bonds. It is likely that a large-scale reconstruction of the glass structure is necessary to remove the terminal structures when the distance between them is relatively large. Hence, the present results suggest that a nitridation strategy is important for the efficient production of oxynitride glasses with highly stable structures by polymerization, as it seems that strong nitridation results in the formation of many terminal structures, such as Si–NH_n, which are not easily removed once formed. Hence, the introduction of nitride ions without the formation of a metastable terminal structure is essential for the efficient production of oxynitride glasses by ammonolysis.

In terms of process optimization for efficient oxynitride formation, it is useful to use a gas mixture for ammonolysis. As can be observed in Fig. S2, the decomposition rate of ammonia strongly depends on Φ_{AM}. Ammonia cracking is known to be a slow reaction.70) As previously mentioned, it is possible that the residual oxygen gas in the furnace plays an important role in nitridation and polymerization. The hydrogen gas concentrations are not shown in Fig. S2 because of instrumental limitations. However, the presence of hydrogen due to the decomposition of ammonia must affect the formation of hydrogen-terminated structures. Hence, consideration of the dynamics of ammonia cracking, not only due to the reacting power but also due to furnace materials, is needed for designing efficient nitridation without forming hydrogen-terminated structures and for the polymerization of the oxynitride glass structures.

Regarding the optical properties, all the powders showed broadband green luminescence upon excitation with ultraviolet light after ammonolysis, as shown in **Fig. 6**(a). The observed PL and PLE profiles indicate that divalent Eu ions (Eu^{2+}) act as luminescence centers. Interestingly, the PLE profile of the powder not prepared by ammonolysis but by heating in a hydrogen atmosphere showed a PLE profile almost equal to that of the other nitrogen-containing powders. However, the shape of its PL spectrum was different from that of the other powders. In fact, the PL bandwidth of PwH was much narrower than that of the powder after ammonolysis.

These results provide two indications: the excited states of Eu^{2+} ion in oxide glass that contribute to radiative recombination are very similar to those in oxynitride glass, and the radiative recombination process of Eu^{2+} in oxide

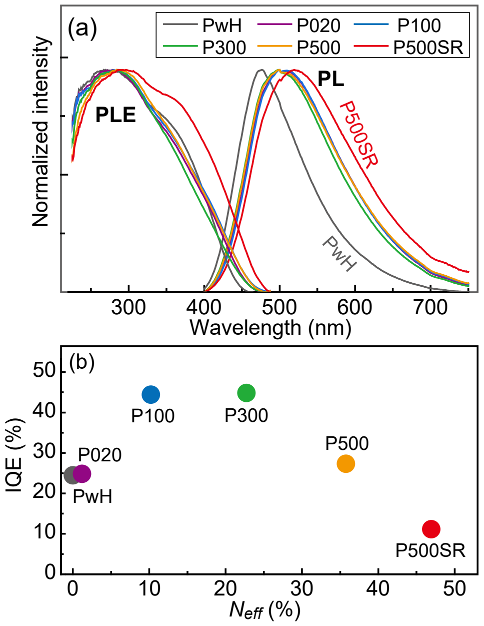

Fig. 6. Photoluminescence (PL) excited by UV light ($\lambda_{ex} = 300\,nm$), and photoluminescence excitation (PLE) spectra monitored at luminescence intensity maximum (a). Internal quantum efficiency as a function of the effective nitrogen concentration (N_{eff}) (b).

glass is different from that in oxynitride glasses. As the tail of the PL spectra at the larger wavelength side is mostly caused by interactions with the vibrational mode,[71–73] the difference in the PL bandwidth between the PwH and oxynitride glasses was likely due to changes in the coordination structure around Eu^{2+}. Although the N_{eff} in P020 was considerably lower than that in P300, the PL peak wavelengths and bandwidths of P020 and P300 were nearly identical. This result indicated that the coordination structure of the radiative Eu^{2+} center was highly specific. Because of the dissimilarity between the PL profiles of PwH and P020, the radiative Eu^{2+} center formed in P020 should have different coordination structures. The PL and PLE spectra of P020 and P300 were similar, although the XPS, NMR, and FT-IR spectra of the two powders exhibited dissimilar profiles. It means that Si–N bonds were changed according to Φ_{AM} but the luminescence profile remained unchanged. These results indicate that only Eu ions with specific coordination structures involving nitride ions become radiative Eu^{2+} centers. Notably, the PL profile of P500SR was much broader than those of the other oxynitride glass powders. This may indicate that the radiative recombination process at the Eu^{2+} ion was affected by the presence of thermal structures, such as –Si–N–H.

Figure 6(b) shows the IQE of the Eu^{2+} luminescence in the powders prepared under different ammonolysis conditions. Notably, the IQE seems to reach a maximum in the N_{eff} range of 10–20 %. As mentioned above, the chemical state of Si exhibits systematic changes corresponding to N_{eff}. However, the luminescence efficiency exhibits a different trend from that of N_{eff}. Hence, the degree of nitridation and modification of the chemical state of Si are not simple measures for enhancing the radiative recombination at the Eu^{2+} center. In addition, the IQE of P500SR was significantly lower than those of the other powders. Furthermore, the PL spectrum of P500SR was significantly broader than those of the other powders. It can also be presumed that a high concentration of –Si–NH_m causes luminescence quenching of the Eu^{2+} centers.

Before concluding the discussion, the prospective strategy for efficient luminescence with Eu^{2+} centers should be mentioned. Because the maximum IQE in the previous study[30)] was obtained after long-term thermal treatment of the film with a relatively low N_{eff}, we can expect that a longer ammonolysis period with suitable nitridation activity, likely a condition for P100 or P300, may enable us to obtain a higher IQE of Eu^{2+} luminescence.

4. Conclusion

We examined the synthesis of Si–Al–Sr–Eu–O–N glass powder using a sol–gel process followed by ammonolysis. It was indicated that a relatively high ammonia flow rate, Φ_{AM}, in ammonolysis and ammonolysis at a relatively low temperature induced higher N_{eff} in the resultant glasses. The results of NMR measurements indicated that the nitride ion incorporated in the oxynitride glass was the nearest neighbor to silicon, and XPS results suggested that the chemical state of silicon is highly sensitive to N_{eff}. However, the chemical composition analyzed by XRF showed an obvious anion excess, indicating the formation of terminal structures in the form of –Si–CH_n and –Si–NH_m. The presence of those terminal structures was confirmed by FT-IR measurements. Subsequent thermal analysis indicated that glass with a high N_{eff} is thermally unstable and undergoes thermal decomposition, and that complete removal of these terminal structures takes time. The obtained results suggest a strategy for enhancing the Eu^{2+} luminescence in oxynitride glass, that is, the removal of excess anions, which is likely due to the presence of N–H components. For the utilization of oxynitride glasses in practical applications, it has been suggested that a nitridation process contributing to polymerization involving nitride ions without the formation of terminal structures such as –Si–NH_m, is highly desirable. We expect that further consideration for controlling the nitridation atmosphere, such as the use of a gas mixture for simultaneous control of the oxygen partial pressure and nitridation activity, will enable the efficient production of highly functionalized oxynitride glasses.

Acknowledgements Part of this study will be incorporated into the Ph.D. thesis of LX. Part of this study was conducted at the Tokodai Institute for Elemental Strategies with support from Grant Number JPMXP0112101001 and the Data-Driven Materials Research Institute for Electronics with support from JPMXP1122683430. The XPS and NMR measurements were performed at Research Network and Facility Services Division, NIMS, under support from the ARIM program, Nos. JPMXP1225NM5319 and JPMXP1223NM5260, respectively.

References

1) K. M. Youssef, A. J. Zaddach, C. Niu, D. L. Irving and C. C. Koch, *Mater. Res. Lett.* 3, 95 (2015). https://doi.org/10.1080/21663831.2014.985855.

2) D. Kumar, R. Seetharam and K. Ponappa, *J. Alloy. Compd.* 972, 172732 (2024). https://doi.org/10.1016/j.jallcom.2023.172732.

3) K. Maeda, F. Takeiri, G. Kobayashi, S. Matsuishi, H. Ogino, S. Ida, T. Mori, Y. Uchimoto, S. Tanabe, T. Hasegawa, N. Imanaka and H. Kageyama, *B. Chem. Soc. Jpn.* 95, 26 (2022). https://doi.org/10.1246/bcsj.20210351.

4) J. J. Xu and K. Wu, *Coordin. Chem. Rev.* 486, 215139 (2023). https://doi.org/10.1016/j.ccr.2023.215139.

5) X. Chen and K. M. Ok, *Chem. Sci.* 13, 3942 (2022). https://doi.org/10.1039/D1SC07121A.

6) Y.-F. Shi, W.-B. Wei, X.-T. Wu, H. Lin and Q.-L. Zhu, *Dalton T.* 50, 4112 (2021). https://doi.org/10.1039/D1DT00222H.

7) X. Chen and K. M. Ok, *Chem. Sci.* 13, 3942 (2022). https://doi.org/10.1039/D1SC07121A.

8) R. Xie, N. Hirosaki, M. Mitomo, Y. Yamamoto, T. Suehiro and N. Ohashi, *J. Am. Ceram. Soc.* 87, 1368 (2004). https://doi.org/10.1111/j.1151-2916.2004.tb07738.x.

9) N. Hirosaki, R.-J. Xie, K. Kimoto, T. Sekiguchi, Y. Yamamoto, T. Suehiro and M. Mitomo, *Appl. Phys. Lett.* 86, 1 (2005). https://doi.org/10.1063/1.1935027.

10) D. Wen, H. Kato and M. Kakihana, *ACS Sustain. Chem. Eng.* 8, 12286 (2020). https://doi.org/10.1021/acssuschemeng.0c04389.

11) D. Wen, H. Liu, Z. Ma, L. Zhou, J. Li, Y. Guo, Q. Zeng, P. A. Tanner and M. Wu, *Angew. Chem. Int. Edit.* 62, e202307868 (2023). https://doi.org/10.1002/anie.202307868.

12) J. I. Yamaura, S. Maki, T. Honda, Y. Matsui, A. Noviyanto, T. Otomo, H. Abe, Y. Murakami and N. Ohashi, *Chem. Commun.* 56, 1385 (2020). https://doi.org/10.1039/c9cc07029j.

13) F. Oehler, H. T. Langhammer and S. G. Ebbinghaus, *J. Eur. Ceram. Soc.* 37, 2129 (2017). https://doi.org/10.1016/j.jeurceramsoc.2016.12.030.

14) A. Hosono, Y. Masubuchi, T. Endo and S. Kikkawa, *Dalton T.* 46, 16837 (2017). https://doi.org/10.1039/C7DT03765A.

15) L. Mao, X. Cai, H. Gao, X. Diao and J. Zhang, *Nano Energy* 39, 172 (2017). https://doi.org/10.1016/j.nanoen.2017.06.026.

16) H. Banno, S. Funahashi, T. Asaka, N. Hirosaki and K. Fukuda, *J. Solid State Chem.* 230, 149 (2015). https://doi.org/10.1016/j.jssc.2015.06.043.

17) J. Podwórny, A. Pawełek and J. Czechowski, *Powder Diffr.* 32, S2 (2017). https://doi.org/10.1017/S088571561700001X.

18) K. Fukui, S. Iimura, A. Iskandarov, T. Tada and H. Hosono, *J. Am. Chem. Soc.* 144, 1523 (2022). https://doi.org/10.1021/jacs.1c11353.

19) S. Yamamoto, Y. Ohashi, Y. Masubuchi, T. Takeda, T. Motohashi and S. Kikkawa, *J. Alloy. Compd.* 482, 160 (2009). https://doi.org/10.1016/j.jallcom.2009.03.151.

20) J. Li, Y. Jiang, Z. Zhang, M. Tsuji, M. Miyazaki, M. Kitano and H. Hosono, *Adv. Energy Mater.* 13, 2302424 (2023). https://doi.org/10.1002/aenm.202302424.

21) A. Noviyanto, T. Nishimura, M. Kitano and N. Ohashi, *J. Eur. Ceram. Soc.* 36, 4083 (2016). https://doi.org/10.1016/j.jeurceramsoc.2016.06.031.

22) M. Namba, H. Takatsu, H.-B. Li, K. Murayama, R. Terada, Q. Yang, T. Terashima, H. Ohta and H. Kageyama, *Chem. Mater.* 36, 2076 (2024). https://doi.org/10.1021/acs.chemmater.3c03178.

23) J. Lee, Q. Zhang and F. Saito, *Ind. Eng. Chem. Res.* 40, 4785 (2001). https://doi.org/10.1021/ie010086k.

24) N. Arumugam, A. Hönnerscheid and M. Jansen, *Z. Anorg. Allg. Chem.* 629, 939 (2003). https://doi.org/10.1002/zaac.200200452.

25) Y. Hinuma, A. Grüneis, G. Kresse and F. Oba, *Phys. Rev. B* 90, 155405 (2014). https://doi.org/10.1103/PhysRevB.90.155405.

26) A. Duval, P. Houizot and T. Rouxel, *J. Am. Ceram. Soc.* 106, 1611 (2023). https://doi.org/10.2109/jcersj2.18097.

27) H. Hyuga, *J. Ceram. Soc. Jpn.* 126, 968 (2018). https://doi.org/10.2109/jcersj2.18097.

28) K. Watari, H. J. Hwang, M. Toriyama and S. Kanzaki, *J. Mater. Res.* 14, 1409 (1999). https://doi.org/10.1557/JMR.1999.0191.

29) S. Watanabe, Y. Osawa, S. Machida, K. Katsumata, A. Yasumori, K. Takahashi, K. Deguchi, S. Ohki and H. Segawa, *J. Non-Cryst. Solids* 573, 121107 (2021). https://doi.org/10.1016/j.jnoncrysol.2021.121107.

30) X. Liu, T. Ohsawa, J. Xu, M. Yanagida, K. Takahashi, T. Takeda, T. Kishi, T. Yano, H. Segawa and N. Ohashi, *J. Mater. Chem. C* 13, 18286 (2025). https://doi.org/10.1039/D5TC01527H.

31) H. Segawa, N. A. Wójcik, K. Takahashi, T. Takeda and S. Ali, *J. Am. Ceram. Soc.* 107, 2930 (2024). https://doi.org/10.1111/JACE.19615.

32) H. Segawa and N. Hirosaki, *Ceram. Int.* 44, 4783 (2018). https://doi.org/10.1016/j.ceramint.2017.12.063.

33) S. Li, L. Wang, D. Tang, Y. Cho, X. Liu, X. Zhou, L. Lu, L. Zhang, T. Takeda, N. Hirosaki and R.-J. Xie, *Chem. Mater.* 30, 494 (2018). https://doi.org/10.1021/acs.chemmater.7b04605.

34) R. E. Loehman, *J. Non-Cryst. Solids* 42, 433 (1980). https://doi.org/10.1016/0022-3093(80)90042-3.

35) H. Schmidt, M. Gupta and M. Bruns, *Phys. Rev. Lett.* 96, 055901 (2006). https://doi.org/10.1103/PhysRevLett.96.055901.

36) H. Haneda, T. Ohgaki, I. Sakaguchi, H. Ryoken, N. Ohashi and A. Yasumori, *Appl. Surf. Sci.* 252, 7265 (2006). https://doi.org/10.1016/j.apsusc.2006.02.179.

37) A. Hosono, Y. Masubuchi and S. Kikkawa, *Ceram. Int.* 43, 2737 (2017). https://doi.org/10.1016/j.ceramint.2016.11.101.

38) Y.-R. Zhang, T. Motohashi, Y. Masubuchi and S. Kikkawa, *J. Eur. Ceram. Soc.* 32, 1269 (2012). https://doi.org/10.1016/j.jeurceramsoc.2011.12.001.

39) S. Kikkawa, S. Sun, Y. Masubuchi, Y. Nagamine and T. Shibahara, *Chem. Mater.* 28, 1312 (2016). https://doi.org/10.1021/acs.chemmater.5b04149.

40) A. Hosono, S.-K. Sun, Y. Masubuchi and S. Kikkawa, *J. Eur. Ceram. Soc.* 36, 3341 (2016). https://doi.org/10.1016/j.jeurceramsoc.2016.05.006.

41) Y. Masubuchi, S. Ohtaki, K. Fujii, M. Yashima, M. Higuchi and S. Kikkawa, *J. Eur. Ceram. Soc.* 40, 6288 (2020). https://doi.org/10.1016/j.jeurceramsoc.2019.10.004.

42) A. Hosono, M. Inoguchi, Y. Masubuchi, K. Murayama, M. Iha, M. Higuchi and S. Kikkawa, *J. Eur. Ceram. Soc.* 40, 2317 (2020). https://doi.org/10.1016/J.JEURCERAMSOC.2020.02.008.

43) Y. Osawa, K. Iwasaki, T. Nakanishi, A. Yasumori, Y. Matsui, T. Nishimura, T. Ohsawa, H. Segawa and N. Ohashi, *J. Am. Ceram. Soc.* 104, 4420 (2021). https://doi.org/10.1111/JACE.17836.

44) R. K. Brow, C. G. Pantano and D. C. Boyd, *J. Am. Ceram. Soc.* 67, c72 (1984). https://doi.org/10.1111/J.1151-2916.1984.TB18834.X.

45) K. Szaniawska, L. Murawski, R. Pastuszak, M. Walewski and G. Fantozzi, *J. Non-Cryst. Solids* 286, 58 (2001). https://doi.org/10.1016/S0022-3093(01)00478-1.

46) B. E. Warren, *Chem. Rev.* 26, 237 (1940). https://doi.org/10.1021/cr60084a007.

47) H. W. Nesbitt, G. M. Bancroft, G. S. Henderson, R. Ho, K. N. Dalby, Y. Huang and Z. Yan, *J. Non-Cryst. Solids* 357, 170 (2011). https://doi.org/10.1016/J.JNONCRYSOL.2010.09.031.

48) G. Pintori and E. Cattaruzza, *Opt. Mater.* 13, 100108 (2022). https://doi.org/10.1016/J.OMX.2021.100108.

49) J. F. Moulder and J. Chastain, “Handbook of X-ray Photoelectron Spectroscopy: A Reference Book of Standard Spectra for Identification and Interpretation of XPS Data”, Physical Electronics Division, Perkin-Elmer Corp. (1992).

50) K. Kawashima, M. Hojamberdiev, O. Mabayoje, B. R. Wygant, K. Yubuta, C. B. Mullins, K. Domen and K. Teshima, *CrystEngComm* 19, 5532 (2017). https://doi.org/10.1039/C7CE00614D.

51) B. Li, Y. Adachi, J. Li, H. Okushi, I. Sakaguchi, S. Ueda, H. Yoshikawa, Y. Yamashita, S. Senju, K. Kobayashi, M. Sumiya, H. Haneda and N. Ohashi, *Appl. Phys. Lett.* 98, 082101 (2011). https://doi.org/10.1063/1.3556440.

52) S. Hirose, S. Ueda and N. Ohashi, *J. Appl. Phys.* 125, 95301 (2019). https://doi.org/10.1063/1.5066574/156311.

53) K. R. Carduner, R. O. Carter, M. E. Milberg and G. M. Crosbie, *Anal. Chem.* 59, 2794 (1987). https://doi.org/10.1021/ac00150a015.

54) C. Cozzan, K. J. Griffith, G. Laurita, J. G. Hu, C. P. Grey and R. Seshadri, *Inorg. Chem.* 56, 2153 (2017). https://doi.org/10.1021/acs.inorgchem.6b02780.

55) R. van Weeren, E. A. Leone, S. Curran, L. C. Klein and S. C. Danforth, *J. Am. Ceram. Soc.* 77, 2699 (1994). https://doi.org/10.1111/j.1151-2916.1994.tb04664.x.

56) C. I. Merzbacher, B. L. Sherriff, J. S. Hartman and W. B. White, *J. Non-Cryst. Solids* 124, 194 (1990). https://doi.org/10.1016/0022-3093(90)90263-L.

57) S. Watanabe, Y. Osawa, S. Machida, K. Katsumata, A. Yasumori, K. Takahashi, K. Deguchi, S. Ohki and H. Segawa, *J. Non-Cryst. Solids* 573, 121107 (2021). https://doi.org/10.1016/J.JNONCRYSOL.2021.121107.

58) Z. Zhao, D. Xiao, K. Chen, R. Wang, L. Liang, Z. Liu, I. Hung, Z. Gan and G. Hou, *ACS Central Sci.* 8, 795 (2022). https://doi.org/10.1021/acscentsci.1c01497.

59) S. Sakka, *J. Non-Cryst. Solids* 181, 215 (1995). https://doi.org/10.1016/S0022-3093(94)00514-1.

60) N. Hirosaki, C. Kocer, S. Ogata and K. Tatsumi, *Phys. Rev. B* 71, 104105 (2005). https://doi.org/10.1103/PhysRevB.71.104105.

61) E. Leonova, A. S. Hakeem, K. Jansson, B. Stevensson, Z. Shen, J. Grins, S. Esmaeilzadeh and M. Edén, *J. Non-Cryst. Solids* 354, 49 (2008). https://doi.org/10.1016/j.jnoncrysol.2007.07.027.

62) A. Bertoluzza, C. Fagnano, M. Antonietta Morelli, V. Gottardi and M. Guglielmi, *J. Non-Cryst. Solids* 48, 117 (1982). https://doi.org/10.1016/0022-3093(82)90250-2.

63) H. Aguiar, J. Serra, P. González and B. León, *J. Non-Cryst. Solids* 355, 475 (2009). https://doi.org/10.1016/J.JNONCRYSOL.2009.01.010.

64) A. Bertoluzza, C. Fagnano, M. Antonietta Morelli, V. Gottardi and M. Guglielmi, *J. Non-Cryst. Solids* 48, 117 (1982). https://doi.org/10.1016/0022-3093(82)90250-2.

65) B. T. Poe, P. F. McMillan, C. A. Angell and R. K. Sato, *Chem. Geol.* 96, 333 (1992). https://doi.org/10.1016/0009-2541(92)90063-B.

66) H. Ono, T. Ikarashi, Y. Miura, E. Hasegawa, K. Ando and T. Kitano, *Appl. Phys. Lett.* 74, 203 (1999). https://doi.org/10.1063/1.123293.

67) M. Klanjšek Gunde and M. Maček, *Phys. Status Solidi A* 183, 439 (2001). https://doi.org/10.1002/1521-396X(200102)183:2<439::AID-PSSA439>3.0.CO;2-B.

68) K. Kamiya, M. Ohya and T. Yoko, *J. Non-Cryst. Solids* 83, 208 (1986). https://doi.org/10.1016/0022-3093(86)90068-2.

69) J. Szépvölgyi, I. Mohai and J. Gubicza, *J. Mater. Chem.* 11, 859 (2001). https://doi.org/10.1039/b008429h.

70) H. Mizoguchi, Y. Osawa, M. Sasase, N. Ohashi, M. Kitano and H. Hosono, *J. Phys. Chem. Lett.* 14, 9516 (2023). https://doi.org/10.1021/ACS.JPCLETT.3C02446.

71) J. Bouquiaux, S. Poncé, Y. Jia, A. Miglio, M. Mikami and X. Gonze, *Chem. Mater.* 35, 5353 (2023). https://doi.org/10.1021/acs.chemmater.3c00537.

72) R. Shafei, P. J. Strobel, P. J. Schmidt, D. Maganas, W. Schnick and F. Neese, *Phys. Chem. Chem. Phys.* 26, 6277 (2024). https://doi.org/10.1039/D3CP06039J.

73) R. Shafei, P. J. Strobel, P. J. Schmidt, D. Maganas, W. Schnick and F. Neese, *J. Phys. Chem. C* 129, 1495 (2025). https://doi.org/10.1021/acs.jpcc.4c06912.